CHAPTER 3

MATHEMATICAL MODELLING

3.1 Overview

Present chapter explores into the mathematical modelling of FPSRS. It begins by discussing the derived solar radiation equations to understanding solar irradiance's role in FPSRS design. The discussion focuses on the three-dimensional geometric analytical equations that are specifically utilized to comprehend the relationship between the beam ray and reflector interaction in FPSRS. The mathematical modelling of FPSRS is thoroughly outlined form the process basic ray tracing principles to complex computational techniques for simulating solar rays within the system. The steps involved in tracing a particular ray that includes the calculation of different solar rays' angle, reflectivity (ρ), and the influence of system geometry on performance, are meticulously described. Through detailed mathematical modelling, this section aims to provide a comprehensive understanding of the dynamics within FPSRS. It serves as a foundation for predictive analysis of system performance across different environmental scenarios, underpinning the development of efficient and cost-effective solar thermal energy solutions.

3.2 Solar beam rays reflection from various angled surfaces

Sun rays reach the Earth's surface in two primary forms: beam rays and diffuse rays. Beam rays are characterized by their direct and scattered path and play a significant role in solar radiation heat transfer. These rays travel in a straight line and have the highest amount of solar energy compared to diffuse rays (Rehman, 2019). On the other hand, diffuse rays result from sunlight scattering in the Earth's atmosphere. Understanding this differentiation is crucial for designing and optimizing solar energy systems and it influencing the efficiency as well as the performance of STSs (Bellos & Tzivanidis, 2019b). The method and equation used to calculate the intensity of solar beam ray on the Earth's horizontal surface is discussed in the following discussion.

The pictorial representation of the angle made by the solar bema ray to the horizontal surface is shown in the Fig. 3.1 (John A. Duffi, 1989). Where Fig. 3.1 (a) shows the all possible angle while solar beam ray is reflected back from the inclined surface. The pictorial view of zenith angle zenith angle (γ) is shown in Fig. 3.1 (b). The amount of radiation received at the outer atmosphere of the earth is calculated with help of Eq. (3.1) (John A. Duffi, 1989), where G_{on} is represented as the extra-

terrestrial radiation measured on the plane normal to the radiation on n^{th} day (W/m^2), G_s is represented as the solar constant (W/m^2), n is represents as the number of day from the chose year and δ represents the declination angle.

$$G_{on} = \begin{cases} G_{sc}\left(1 + 0.033\cos\frac{360n}{365}\right) \\ G_{sc}(1.000110 + 0.034221\cos\delta + 0.001280\sin\delta + \ 0.000179\cos 2\delta + 0.000077\sin 2\delta) \end{cases} \quad (3.1)$$

The δ and the angle of inclination (θ) can be calculated with use of Eq. (3.2) and Eq. (3.3) simultaneously (Duffie et al., 1985). Where, Φ represents the angle between reflector and horizontal surface, β represents the angle with reflected ray and normal of the reflecting plane, θ_H is represented as the angle between beam ray and the horizontal surface and ω represents the hour angle.

$$\delta = 23.45\sin\left(360\frac{284+n}{365}\right) \quad (3.2)$$

$$\cos\theta = \sin\Phi\left(\begin{matrix}\sin\delta_d \cdot \cos\beta \\ +\cos\delta_d \cdot \cos\gamma \cdot \cos\omega \cdot \sin\beta\end{matrix}\right) + \cos\Phi\left(\begin{matrix}\cos\delta_d \cdot \cos\omega \cdot \cos\beta - \\ \sin\delta_d \cdot \cos\gamma \cdot \sin\beta\end{matrix}\right) + \cos\delta_d \cdot \sin\gamma \cdot \sin\omega \cdot \sin\beta \quad (3.3)$$

In actual practice there may be horizontal (β=0°) or vertical (β=90°) solar radiation receiving surfaces, in that case Eq. (3.4) and Eq. (3.5) helps to find the value of θ (Smith & Rohatgi, 1993).

$$\cos\theta = -\sin\delta\cos\Phi\cos\gamma + \cos\delta\sin\Phi\cos\gamma\cos\omega + \cos\delta\sin\gamma\sin\omega \quad (3.4)$$

$$\cos\theta_z = \cos\Phi\cos\delta\cos\omega + \sin\phi\sin\delta \quad (3.5)$$

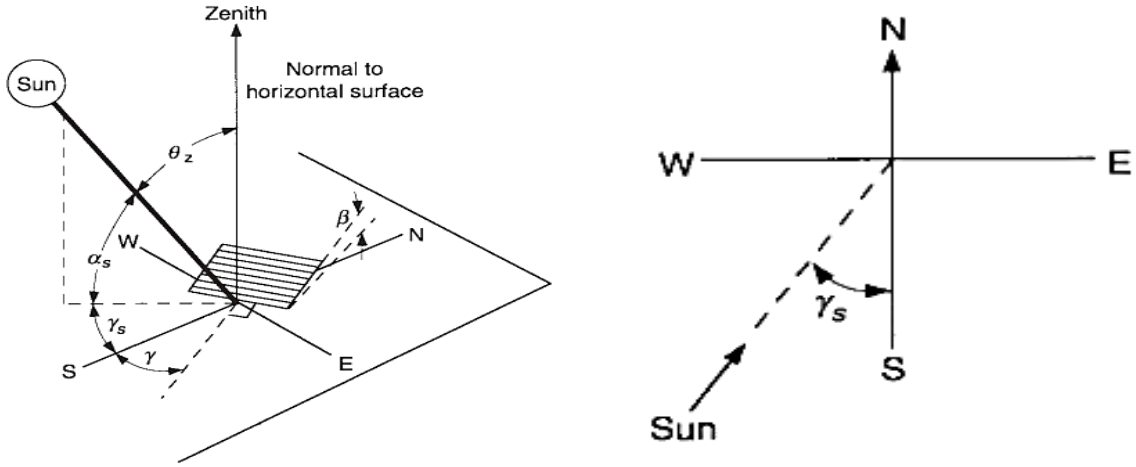

(a) (b)

Fig. 3.1 angle made by the solar beam ray to the (a) inclined plane and (b)zenith angle (John A. Duffi, 1989)

For purposes of solar process design and performance calculations, it is often necessary to calculate the hourly radiation on a tilted surface of a collector from measurements or estimates of solar radiation on a horizontal surface. For better calculation of the study and to get insight data following quantities will helps. In which the value of solar azimuth angle (γ_s) will be calculated by using Eq. (3.6) (Duffie et al., 1985).

$$\gamma_s = \text{sign}(\omega) \left| \cos^{-1} \left(\frac{\cos\theta_z \sin\phi - \sin\delta}{\sin\theta_z \cos\phi} \right) \right| \tag{3.6}$$

The geometric factor (R_b) can be define as the ratio of beam radiation on the tilted surface to that on a horizontal surface at any time and it can be calculated exactly by using the Eq. (3.7) (Schüler et al., 2007). Where, the G_b is represent the intensity of beam radiation on horizontal surface (W/m^2) and $G_{b,T}$ is represent the intensity of beam radiation on inclined surface (W/m^2). The value of sunset hour angle (ω_s) can be computed with help of Eq. (3.8) when $\theta_z = 90°$ and N_d is represents as the number of daylight hours which can be solve by using Eq. (3.9) (Schüler et al., 2007). The solar radiation equations discussed above are utilized in solving the mathematical model of the FPSRS, as will be elaborated in the subsequent discussion.

$$R_b = \frac{G_{b,T}}{G_b} = \frac{G_{b,n}\cos\theta}{G_{b,n}\cos\theta_z} = \frac{\cos\theta}{\cos\theta_z} \tag{3.7}$$

$$\cos\omega_s = -\frac{\sin\phi\sin\delta}{\cos\phi\cos\delta} = -\tan\phi\tan\delta \tag{3.8}$$

$$N_d = \frac{2}{15}\cos^{-1}(-\tan\phi\tan\delta) \tag{3.9}$$

3.3 Mathematical modelling of flat plate solar reflecting system

The detailed understanding of the behaviour of a single ray after reflection from the reflectors at different angles is discussed herein. To illustrate this, the present study discuss the FPSRS to explain the concept of solar beam ray's behaviour. Subsequently, the three-dimensional geometric analytical equations specific to FPSRS are explained along with their impact on system efficiency. To gain a good understanding of the ray's dynamic behaviour within the FPSRS, comprehensive mathematical modelling is undertaken. The basic schematic representation of the solar beam ray reflection and movement inside the FPSRS is presented in Fig. 3.2. The ray originates from the Top imaginary surface (TIS), reflects off the Reflector (R) and reaches the Bottom receiving surface

(BRS). However, the details of the mathematical modelling of FPSRS and the characteristic behaviour of the ray after reflection from the reflector are presented in Fig. 3.3 as a schematic diagram. It can be observed that once the ray enters the system from the TIS, its behaviour is analysed. The analysis done according to the reflection from the reflector as well as the final destination of the ray, whether it reaches the BRS or exits the system. Two separate coordinate systems are used: (i) coordinate system-1 at the origin of the FPSRS and (ii) coordinate system-2 at every line and plane intersection, which helps to precisely predict the position of the ray.

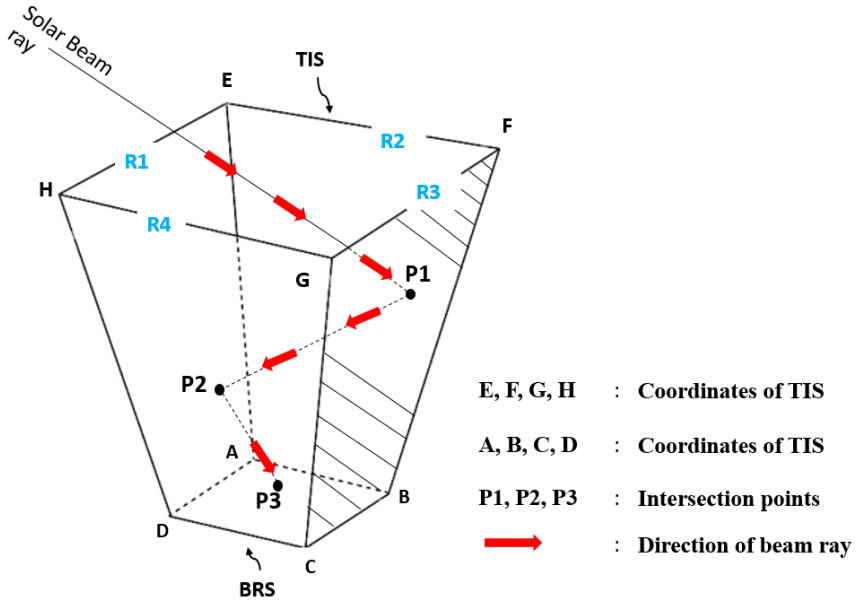

Fig. 3.2 Schematic representation of solar beam ray reflection and the path follow inside the FPSRS.

. The coordinate system-1 functions as the global coordinate system for the mathematical model and serves as the reference coordinate system throughout the calculations. However, coordinate system-2 functions as the local coordinate for the mathematical model and assists in measuring the coordinates of the intersection points of the line and plane and adjusting its coordinates according to the configuration of the system. Following are the few assumptions have been taken to compute the behaviour of the ray like, (i) only beam (direct) solar radiation is considered, (ii) direct solar radiation is assumed to be incident as parallel beams, (iii) the reflection of the beams is not affected by aerosols, dust, or moisture., (iv) optical properties of reflecting surfaces are considered to be constant thought the experiment and (v) all reflective surfaces are treated as perfectly specular and free from deformations (Carrillo-Andrés et al., 2022).

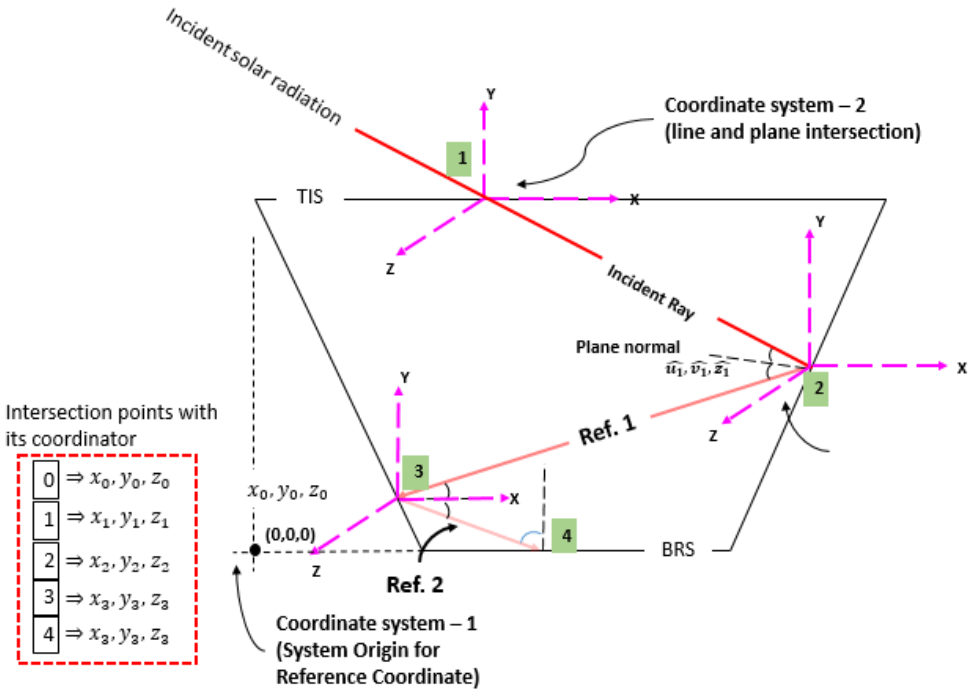

Fig. 3.3 Mathematical model of FPSRS.

To understand the intersection of ray and the reflector and to find the intersecting point the analytical three dimensional geometrical equations can be helped. For that it is assume that the ray is consider to be a line and the reflector is consider to be as a plane. For an instant, with help of three point on the plan like (x_1, y_1, z_1), (x_2, y_2, z_2) and (x_3, y_3, z_3) the geometric plane equation can be obtained from the Eq. (3.10) and the normal of the plane $(\vec{u})$ can be obtained from the Eq. (3.11) (P. R. Vittal, 2013),where i , j and k represent the direction of normal vector and u, v and w represent the coefficient of the line vector.

$$a(x - x_0) + b(y - y_0) + c(z - z_0) = 0 \quad (3.10)$$

$$\vec{u} = \begin{bmatrix} i & j & k \\ u1 & v1 & z1 \\ u2 & v2 & z2 \end{bmatrix} \quad (3.11)$$

However, the line passing through two points named $P_1(x_0, y_0, z_0)$ and $P_2(x_1, y_1, z_1)$ can be derived from the line equations for the three different coordinates x, y, and z, as shown from Eq. (3.12) to Eq. (3.14), respectively (P. R. Vittal, 2013). The variable 't' represents the line coefficient factor, and its value ranges from $0 \leq t \leq 1$, where 0 serves as the starting point of the line and 1 represents the endpoint of the line.

$$x = x_1 + (1 - x_2)t \quad (3.12)$$

$$y = y_1 + (1 - y_2)t \quad (3.13)$$

$$z = z_1 + (1 - z_2)t \quad (3.14)$$

The angle between the two lines (θ_L) can be obtained from the direction vector of that lines and it can be obtained from Eq. (3.15) (Riveros-Rosas et al., 2010). In addition l, m, and n shows the coefficient of lines which make an angle.

$$\theta_L = \cos^{-1}\left(\frac{l_1 l_2 + m_1 m_2 + n_1 n_2}{\sqrt{(l_1^2+m_1^2+n_1^2}.\sqrt{(l_2^2+m_2^2+n_2^2}}\right) \quad (3.15)$$

The performance of the FPSRS is predicted by its thermal performance and optical performance. However, the main focus of the present study is to examine the different shape of the TIS impacts the optical performance of the FPSRS. The Optical concentration ratio (OCR) is a key factor in understanding the significance of the TIS shape on the system's optical performance. The OCR represents the ratio of the number of rays reaching the bottom receiving surface (N_{BRS}) to the number of rays entering from the TIS (N_{TIS}). It can be calculated using Eq. 3.16 (Glassner, 2019).

$$OCR = \frac{N_{BRS}}{N_{TIS}} \quad (3.16)$$

The value of η_{opt} of the FPSRS is computed with use of Eq. 3.17 (Duffie et al., 1985), where I_{BRS} is the solar intensity reached at the receiver area in W/m^2 and I_{TIS} is the solar intensity entering from the TIS in W/m^2, R is reflectivity of the reflector and j is the number of reflection performed by rays.

$$\eta_{opt} = \sum_{j=1}^{N_{TIS}} (I_{BRS} \cdot \delta_R^j) / I_{TIS} \quad (3.17)$$

In addition to above discussion, the radiation model proposed by H. C. Hottel (Hottel, 196 C.E.) to predict the behaviour of ray reflection for grey surfaces and gas can be also used to understand the ray's reflection for the present study. It is important to note that the present investigation focuses solely on surface-to-surface interactions. However, the reflection of rays between surfaces and gas and between different gas components is not taken into consideration. The interchange of radiation between two reflective surfaces is described by Eq. 3.18 (Hottel, 196 C.E.), where $\overline{s_j s_i}$ represents the total interchange area between surface i and surface j in square meters (m²). A_i denotes the area of surface i in square meters (m²), W_i represents the radiation flux leaving surface i in watts per square meter (W/m²), W_i^j represents the total amount of energy interchange between the two surfaces in watts per square meter (W/m²), and δ_{ij} is the *"Kronecker delta"*. The Kronecker delta takes a value of zero except when i=j, in which case its value is 1. Furthermore, $\overline{g_j s_i}$ represents the total interchange area between surface i and gas j, ϵ_i denotes the emissivity of surface i, ρ_i is the

reflectivity of surface i, and E represents the hemispherical black body power in watts per square meter (W/m^2).

For surface zone i to j:

$$j\sum\left(\overline{s_j s_i}-\delta_{ij}\frac{A_i}{\rho_i}\right)W_i+\sum_j \overline{g_j s_i}\ W_i^{\ j}=-\frac{A_i\epsilon_i}{\rho_i}E_i \tag{3.18}$$

Additionally, the same physical phenomenon is considered for surface j and surface i, as shown in Eq. 3.19 (Hottel, 196 C.E.),

For surface zone j to i:

$$i\sum\left(\overline{s_i s_j}-\delta_{ji}\frac{A_j}{\rho_j}\right)W_j+\sum_i \overline{g_i s_j}\ W_j^{i}=-\frac{A_j\epsilon_j}{\rho_j}E_j \tag{3.19}$$

The total interchange area between two surfaces can be calculated using Eq. 3.20 (Hottel, 196 C.E.), where W_j^i is represents the amount of energy exchanged between surface i and surface j.

$$\overline{S_i S_j}=\frac{A_i\epsilon_i}{\rho_i}\left(W_j^i-\delta_{ij}\epsilon_i\right) \tag{3.20}$$

On the other hand, the total interchange area between the gas and the surface can be determined through Eq. 3.21 (Khallaf et al., 2020) where, K being the absorption coefficient, V denoting the system's volume and b representing the ratio of the absorption coefficient to the total extinction coefficient. However, as discussed previously in the present study only surface-to-surface radiation is considered, and therefore, the remaining correlations are not utilized for the calculations,

$$\overline{G_i G_j}=4KV_i\frac{1-b}{b}\left(W_j^i-\delta_{ij}(1-b)\right) \tag{3.21}$$

In Eq. 3.22 (Tsvetkov et al., 2020), the total interchange area between a surface and the gas is obtained, wherein n_i corresponds to either the iteration number or the number of the surface. Nevertheless, since the study exclusively focuses on surface-to-surface radiation, this particular correlation is not applied in the current calculations. This strategy seeks to comprehend how the physical characteristics differ from one another relatively.

$$\overline{S_i G_j}=\frac{A_i\cdot n_i}{\rho_i}W_j^i=4KV_i\frac{1-b}{b}\left(W_j^i\right) \tag{3.22}$$

3.4 Summary

The chapter discusses the mathematical modelling of the FPSRS, aiming to provide a comprehensive understanding of its dynamics. It begins with an exploration of derived solar radiation equations and highlights the role of solar irradiance in STS design. Subsequently, it also delves into three-dimensional geometric analytical equations used for the FPSRS, illustrating the basic schematic diagram of the FPSRS as shown in Fig. 3.2. In detail, the chapter meticulously outlines the steps involved in tracing a particular ray, including calculations of solar angles, ρ, and the influence of system geometry on performance. Through detailed mathematical modelling, the chapter aims to establish a solid foundation for predictive analysis of system performance across various environmental scenarios. This groundwork is crucial for the development of efficient, optimized, and cost-effective STS solutions, facilitating informed decision-making in the field of renewable energy technology.

CHAPTER 4

EXPERIMENTATION OF FPSRS

4.1 Overview

The present chapter discussed the experimentation of the FPSRS to understand the behaviour of a single ray and to study its reflection characteristics. The ray is categorized into six different types, ranging from case A to F, based on the number of reflections that occur and whether it remains within the system to reach the BRS or exits from the TIS. To comprehend and for better understanding the same investigation was conducted using a virtual CAD model of FPSRS. Two methods were utilized to validate the current experimental findings: (1) the proposed single ray approach was validated against experimental work that considered shadow-type tracing methods (Carrillo-Andrés et al., 2022), and (2) the path of the ray was validated with CAD results by calculating the error due to differences in coordinates on the reflector. The uncertainty analysis is then presented, highlighting its significance for the application of flat plate reflectors on a large scale.

4.2 Description of experimental set-up

The experiment discussed in this section is designed to collect first-hand data, which is crucial for understanding the underlying physics and making informed decisions regarding a proposed hypothesis of FPSRS (Diwania et al., 2020; Lv et al., 2023). This section outlines an experimental setup designed to investigate the optical behaviour of a typical FPSRS. The primary aim of this experimental study is to understand the reflection pattern of rays when they are reflected from opposite and neighbouring reflectors. The experiment helps to comprehend the effects of multiple reflections on the intensity of the ray, a crucial aspect requiring detailed investigation. Another objective is to assess the reflector's performance at different times of the day and across seasons by adjusting the angle of the laser light within the experimental setup is vital for simulating various sun positions. In actual practice, measuring and capturing a single ray in the open atmosphere for any STS is difficult. In order to optimize solar reflector designs and ultimately maximize energy capture efficiency, this type of approach is therefore crucial.

To address above mentioned objective, a small-scale model equipped with a FPTRs was constructed and along with a separate 'H'-type stand to support the laser light for the experiment. Fig. 4.1 displays the three-dimensional model of the FPSRS with a wooden 'H'-type stand. This setup

features two vertical pillars, between which a horizontal wooden bar with a rectangular cross-section is securely fixed. The configuration of the horizontal bar is designed to not only hold the laser light but also to allow its rotation to any desired angle. This feature makes it easier to precisely manipulate the laser light's position, which is crucial for the experiment. A thorough examination of the optical behaviour of the beam is made possible by the laser light's movement into the horizontal bar, which is movable in both the X and Y directions.

The FPSRS is designed with a funnel-type solar reflector and it shaped as an inverted frustum of a square pyramid. This design is instrumental in studying the effects of opposite and parallel reflector impact on the system's optical performance. First, the experiment is conducted using the FPSRS configuration having STC. This approach ensures precise ray tracing and facilitates in depth understanding of the behaviour of the rays after reflection. Table 4.1 outlines the default specifications for the experimental setup of the scaled-down model of the FPSRS. It serves as a vital reference for replicating the experimental conditions and ensuring consistency in research. To provide a clearer understanding of the experimental process, Fig. 4.2 illustrates the steps involved in developing the experimental setup and conducting the experiments.

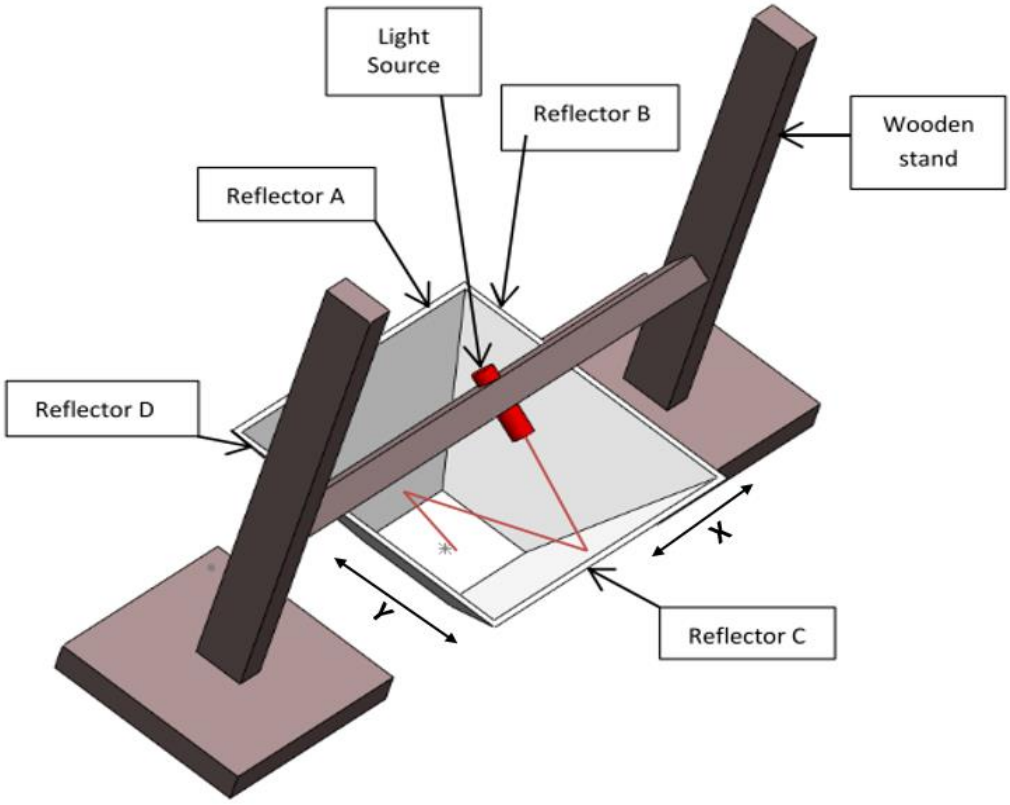

Fig. 4.1 Schematic of experimental set up with FPSRS and laser light in position (J. Patel et al., 2023).

Table 4.1 Default specification of experimental setup

Parameter	Specification	References
Shape of the Top and bottom aperture area (--)	Square	--
Total Number of reflectors	4	--
Number of discretised elements on TIS and BRS	576	(Fossa et al., 2021)
Area of small element (m^2)	2.25×10^{-5}	(Suharta et al., 1996)
Distance between two vertical bar of wooden 'H' stand (m)	1.524	--
Vertical distance at laser light places (m)	0.9144	--
Laser light capacity (W)	0.1	(*Laser Light, Smars®)*
Distance cover by laser light (m)	8046.45	(*Laser Light, Smars®)*
Total TIS aperture area (m^2)	0.8361	(Lin et al., 2013)
A_{BRS} (m^2)	0.0920	(Lin et al., 2013)
H (m)	0.5273	(Huang et al., 2014)
Φ (°)	58.36	(Huang et al., 2014)
ρ (%)	93.45	(Saura et al., 2021)

4.2.1 Methodology

The approach used for the experiments is detailed in this section. The steps involved in developing the entire experimental model of the FPSRS is illustrated in Fig. 4.2. Experiment was conducted in the dark room to ensure proper reflection from the mirrors. Additionally, with the help of overhead projector sheets, all of the mirrors are accurately measured and cut to the required shapes, as shown in Fig. 4.2 (a). As seen in Fig. 4.2 (c), an aluminium carrier is used to precisely hold all four mirrors in place with silicone sealant (Alston industries®) and sealant is used to assure alignment throughout the experimental process. Subsequently, transparent plastic sheets (overheated projector sheet) are utilized to create cells on TIS as well as on BRS. A specific number of data points are defined at the TIS and the rays will impact and continue their trajectory during the experimental runs. The rays will impact and continue on their route during the experimental runs, with a predetermined number of data points established at the TIS. For instance, the TIS is subdivided into 25 rows and 25 columns for clarity, with each intersecting coordinate labelled as (x_o, y_o, z_o), (x_1, y_1, z_1) and so forth. Similarly, the BRS undergoes the same subdivision process, as detailed in Fig. 4.2 (d) and Fig. 4.2 (e) respectively. Finally, the entire FPSRS system is positioned at the base of the wooden 'H'-shaped stand for conducting experiments using laser light in the dark room.

During the experiments a ray is allowed to fall sequentially on the centre of each cell (24 x 24), or sub-division, one-by-one in a particular order. Coordinates of each such impingement of the ray, as it starts traversing from the TIS and until it approaches to the BRS or escaping back from top surface, is systematically recorded. During the experiment the room is kept dark for better

visualisation of the behaviour of the ray by use of a laser light. Every such coordinate's placement at TIS and BRS is meticulously documented and reported for additional examination. In the second stage of the testing, a similar exercise of ray tracing is then developed and carried out in an appropriate CAD software. In this case a virtual scenario was developed for a similar model of FPSRS. The virtual experiment was conducted in similar manner for all the coordinates of each ray corresponding to the experimental. The results are obtained and compared with the corresponding experiment.

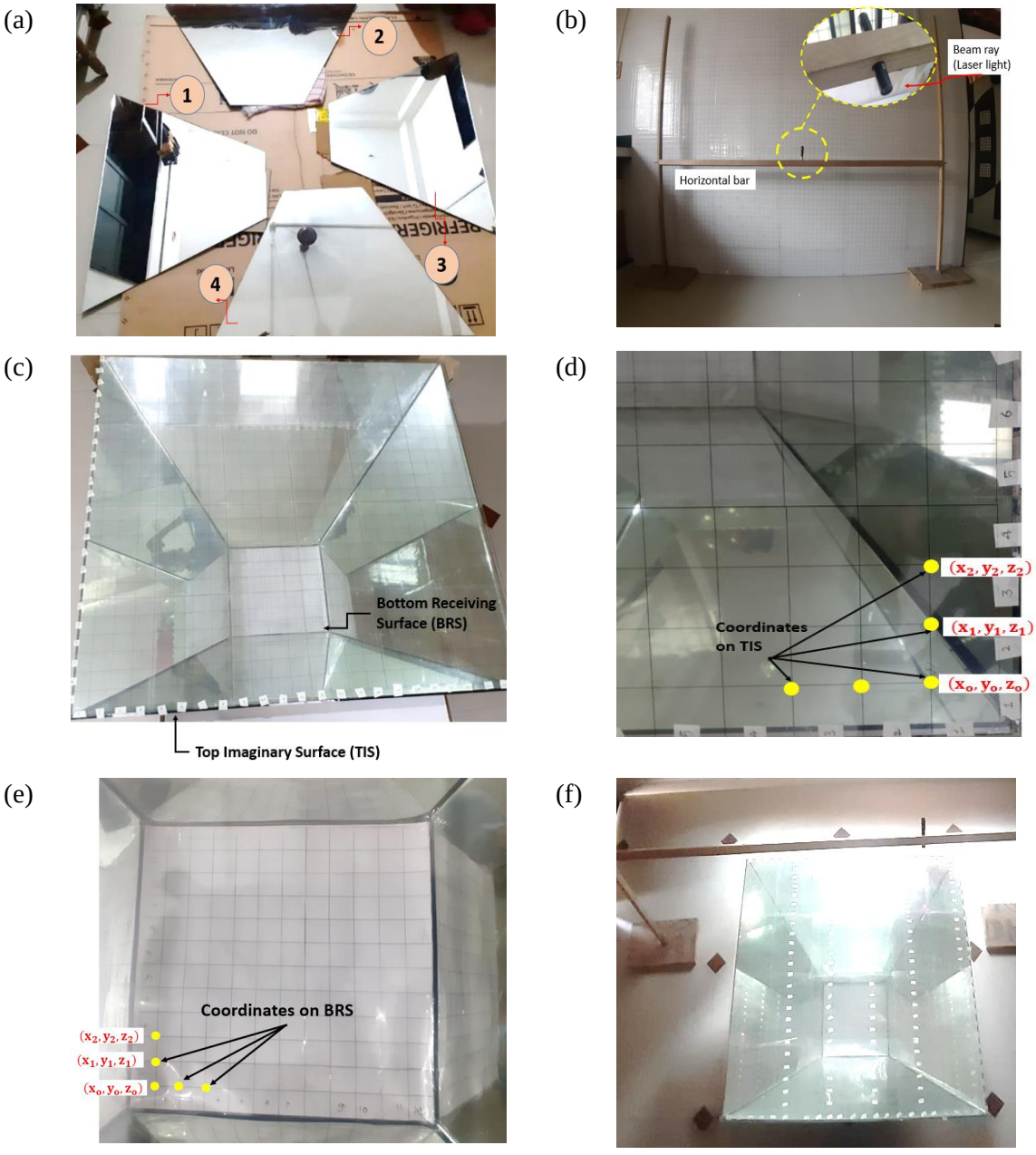

Fig. 4.2 Test setup and making of FPSRS; (a) reflectors, (b) setup with laser light (inset), (c) assembled FPSRS with TIS and BRS, (d) coordinate system at TIS, (e) coordinate system at BRS, and (f) final setup for experiment (J. Patel et al., 2023).

4.2.2 Optical performance

The optical performance of the FPSRS can be understood by evaluating the number of rays reaching the BRS and their intensity levels upon arrival. The rays are divided in to six different types to conduct a systematic optical analysis and for better understanding of ray behaviour. These categories are determined based on the number of reflections made by the rays, the path followed by the ray and whether it remains within the system or exits towards the BRS. The detailed classification is outlined in Table 4.2. From the classification, it is evident that rays reaching the BRS directly are categorized as case A, while those with a single reflection from the opposite reflector before reaching the BRS are classified as case B. Rays undergoing two reflections from opposite reflectors and reaching the BRS are assigned to case C, whereas those reaching the BRS after two reflections but involving neighbouring reflectors are designated as case D.

The case E and case F are allocated for rays that exit from the system without reaching the BRS. In case E, rays undergo two or more reflections before leaving the system from the TIS, whereas in case F, rays exit the system from the TIS after only one reflection. Moreover, for better understanding of the ray's path, the pictorial representation of all classified cases is shown in Fig. 4.3. The purpose of categorizing rays into different categories is to understand their behaviour, particularly in terms of the energy is carried by rays involving opposite and neighbouring reflectors. This classification system is utilized to illustrate the collector optical efficiency, as elaborated upon in the subsequent section.

Table 4.2 Classification of rays' interaction with FPSRS

Case	Description
A	Rays reaching directly at the BRS.
B	Rays reaching at the BRS after one reflection.
C	Rays reaching at the BRS after two reflections.
D	Rays reaching at the BRS via reflection from a neighbouring reflector.
E	Rays never reaching at the BRS even after multiple reflection.
F	Rays never reaching at the BRS but quit the system after one reflection.

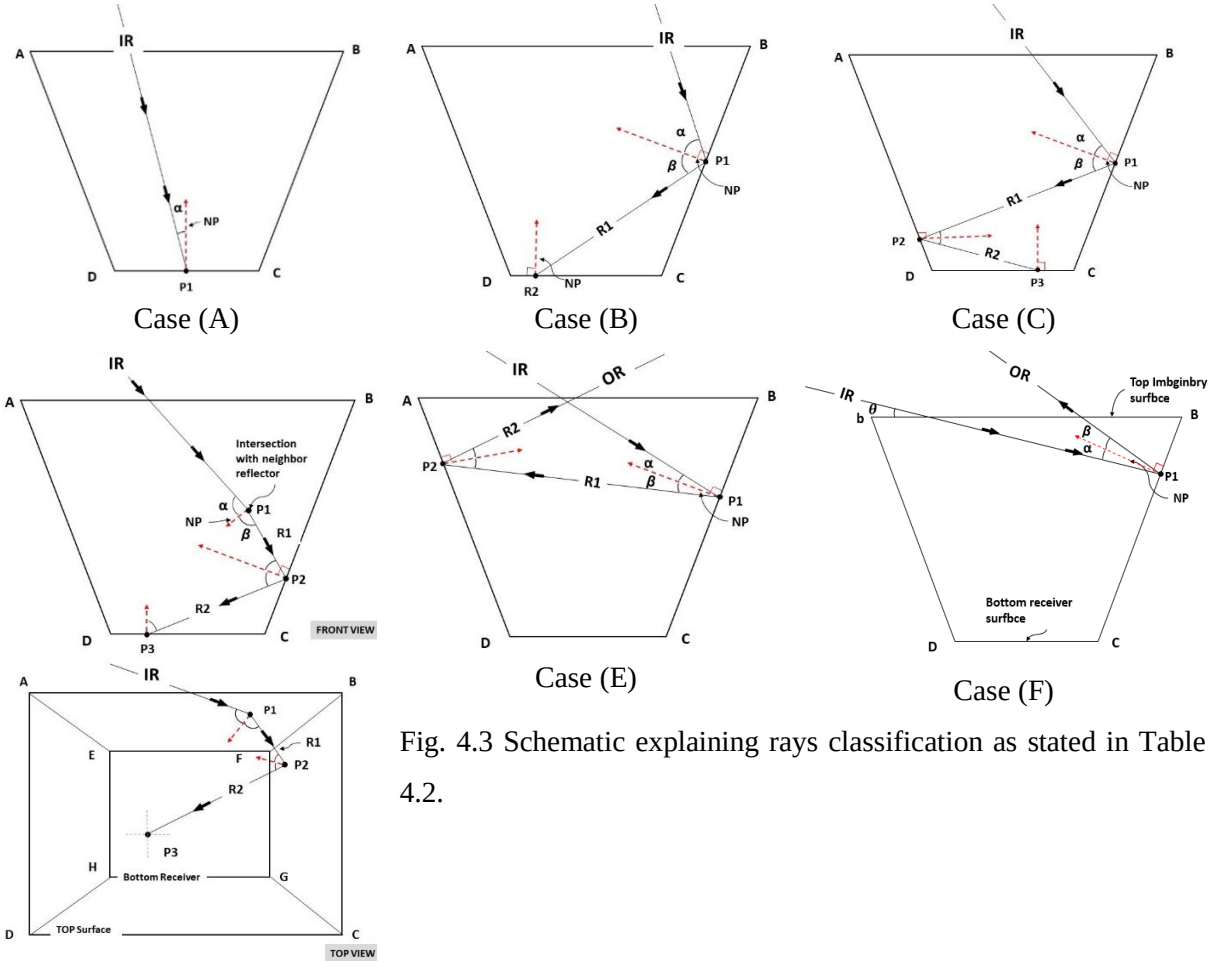

Fig. 4.3 Schematic explaining rays classification as stated in Table 4.2.

The Fig. 4.4 shows a detailed breakdown of rays during the experiment is conducted. The images may exhibit slight contrast due to the low lighting in the experimental room. While conducting the experiment it is observed that while pointing a laser light at different angles towards a particular reflector will not only interact and reflect with the actual image of the laser light point, but it will also reflect the entire surface of the mirror. Hence, a series of virtual images can be observed in almost all the images. The yellow markers are employed to represent the instances of a single ray's reflection on the other reflectors which is not participated in the optical performance of the system. To identify the correct instance of reflection out of many and overcome the issue of multiple reflection, a special arrangement in the set-up is made at the time of the experiments. Under this arrangement the entire surface of non-participating reflectors will be covered or hidden by means of a partially sliding opaque cover. This will hide the surfaces and the laser light is allowed to intersect with only a partially open small area of the surface of the reflector relevant to the reflection. This phenomenon is attributed to the presence of several virtual images of a laser light reflection on the remaining reflectors and also observed during the ray tracing experiment. Such observations shed light on the complex interaction between rays and reflectors in the FPSRS's setup with contributing to a deeper

understanding of optical behaviour. Exploring these intricacies, it helps in refining the design and optimization of solar reflector systems for enhanced energy capture efficiency.

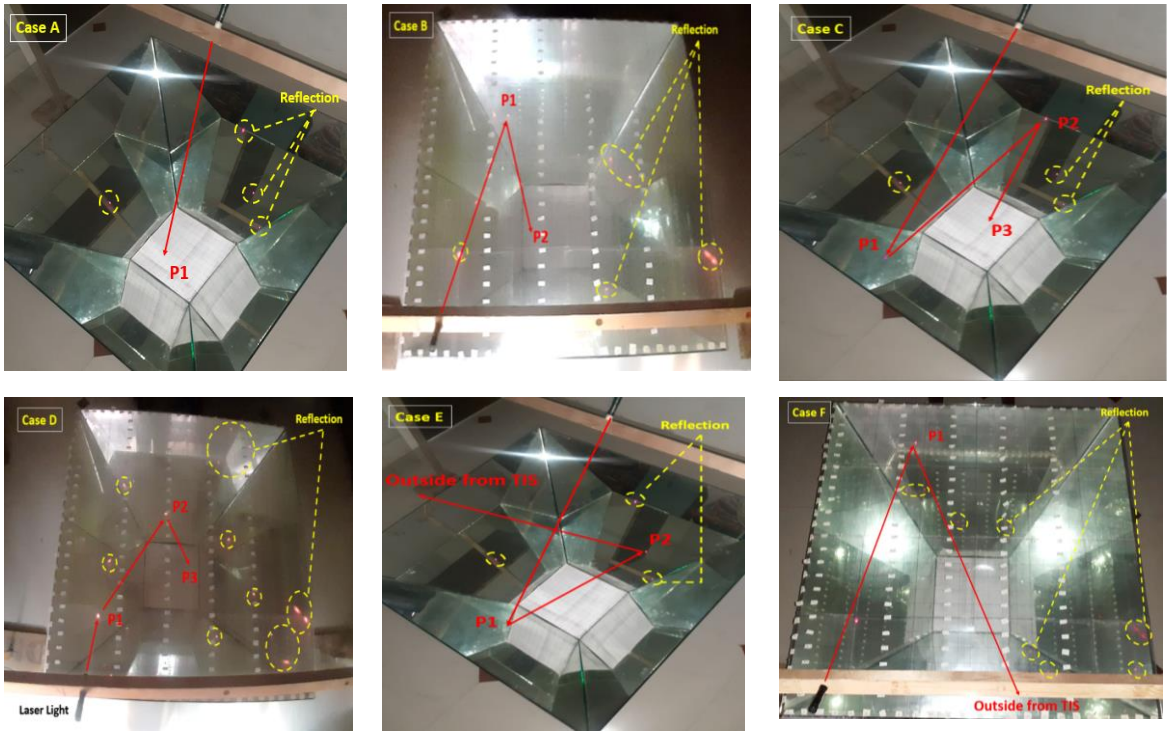

Fig. 4.4 Case wise representation of incident light beam ray's reflection (J. Patel et al., 2023).

In order to understand the contribution of each ray to the overall performance, it is essential to study the ray distribution profile (RDP) at the BRS. The results of RDP on the reflector are also crucial for understanding the optical performance of the FPSRS, as it provides a better understanding of ray distribution on the BRS. The RDP can be defined as the ratio of the number of rays reaching the BRS (N_{BRS}) to the number of rays entering from the TIS (N_{TIS}), and it can be obtained from Eq. (4.1) (J. Patel & Patel, 2023).

$$\text{RDP}(\%) = \frac{\text{No of rays reached at BRS}}{\text{No of ray on TIS}} * 100 \qquad (4.1)$$

Fig. 4.5 presents the RDP for different cases of rays interacting with the FPSRS across varying solar incident angles (θ). The analysis is based on experimental data encompassing a total of 576 rays (arranged in a 24x24 grid) at the TIS of the FPSRS. This data helps in determining the RDP values based on the classification of the rays, as shown in Table 4.2. From the results, it is observed that in case A, as well as case E and F, the type of rays considered to be most actively playing a role in the optical performance represent two extreme conditions in terms of ray behavior within the

system. Case A includes rays that directly reach the BRS and it significantly enhancing the system's performance due to their direct contribution. Conversely, case E and F encompasses rays that exit the system without ever reaching the BRS, thereby contributing nothing to its efficiency. However, rays within cases B, C and D are follow a trajectory that involves multiple reflections off various reflectors before eventually reaching the BRS. This indicates that despite taking indirect paths, these rays still contribute positively to the system's performance.

Besides, a critical observation from Fig. 4.5 shows that the rays in from cases A, B, C, and D are non-existent while $\theta \leq 30°$. The absence of such rays suggests the existence of a specific threshold incident angle below which reflective rays cannot effectively contribute to the BRS. Moreover, as the value of θ increases from 30° to 90°, the presence of cases E and F rays gradually diminishes. This trend indicates an improvement in the η_{opt} of the reflector system at higher value of θ due to effectively reachind of rays to the BRS rather than being lost as in cases E and F. This analysis underscores the importance of understanding the impact of θ on the RDP within FPSRS, offering insights into optimizing the design and orientation of the reflector system for enhanced performance across a range of solar conditions. However, from the experiment, it is challenging to understand the actual reflection of a specific laser point and the path followed by the ray remains unclear. Additionally, accurately measuring the intersection point on the reflector where the laser point intersects poses difficulties. To address this issue, employing a CAD model of the FPSRS proves beneficial in comprehending the ray's trajectory and obtaining real-time data of intersection points on the reflectors and the BRS. The CAD model offers a detailed virtual representation of the system, allowing for precise analysis and visualization of ray paths.

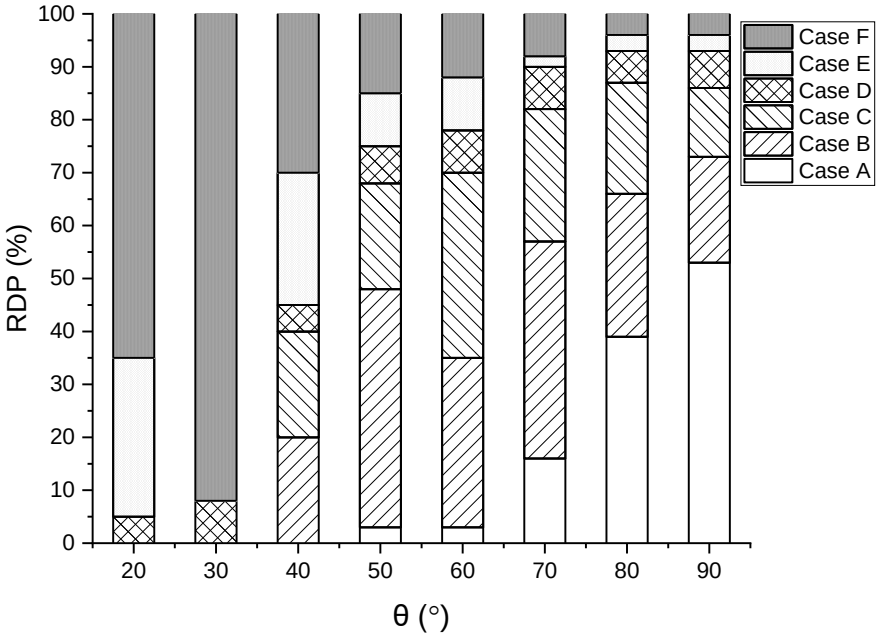

Fig. 4.5 RDP for different cases (A-F) with change in the value of θ from 20° to 90°

4.2.3 CAD model of FPSRS

The CAD model of the FPSRS is played very important role for understaiding of the solar ray dynamics and providing a precise virtual representation of the entire system. It enhances the visualization of each ray's trajectory with enabling accurate determination of intersection points on both the reflectors and the BRS. This capability not only deepens our understanding of the system's optical behavior but also helps in optimizing reflector design for maximum efficiency. Fig. 4.6 (a) displays the basic isometric view of the used STC-based FPSRS CAD model, including the TIS and BRS locations. Reflectors R1, R2, R3, and R4 are crucial for directing solar rays towards the BRS. A core point on the TIS is highlighted for clarity on the initial solar ray interaction. While, Fig. 4.6 (b) shows an isometric view with all supporting planes and the actual ray-carrying plane, emphasizing the importance of these elements in tracing rays' paths and determining their intersection points on the reflectors.

In the CAD model, lines are considered rays, and planes are considered reflectors. This simplification helps in studying the interaction between light and reflective surfaces. Supporting planes are critical for tracing the rays' trajectory to their destination, providing insights into the reflection and refraction processes within the FPSRS. However, the ray-carrying plane, helps to understand the rays' direction after reflection from the different reflectors. The top view is presented in Fig. 4.6 (c), offers a detailed perspective of the rays' paths from their entry on the TIS to their final destinations. This view facilitates a better understanding of the reflector designs' efficiency and effectiveness where, ISP is represented as the intersecting point on reflector.

Fig. 4.6 CAD Model of FPSRS with STC, (a) isometric view with hidden supporting plane, (b) isometric view showing supporting and other planes and (c) top view with similar planes

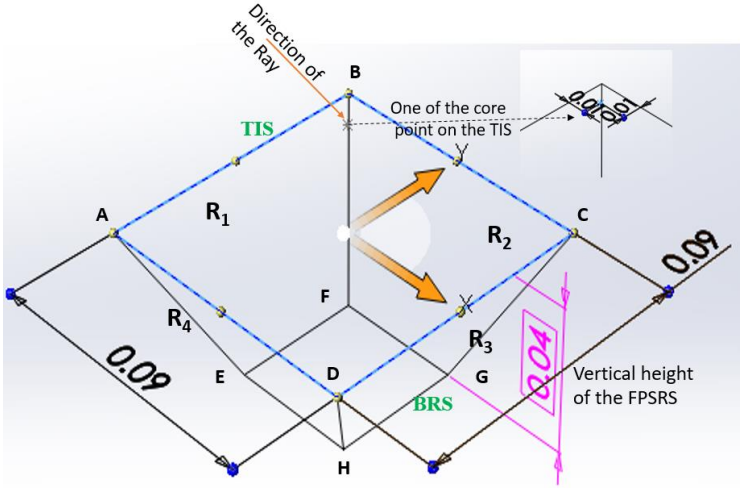

(a)

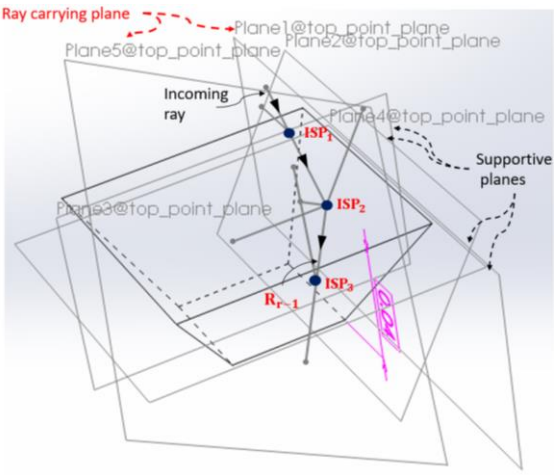

(b)

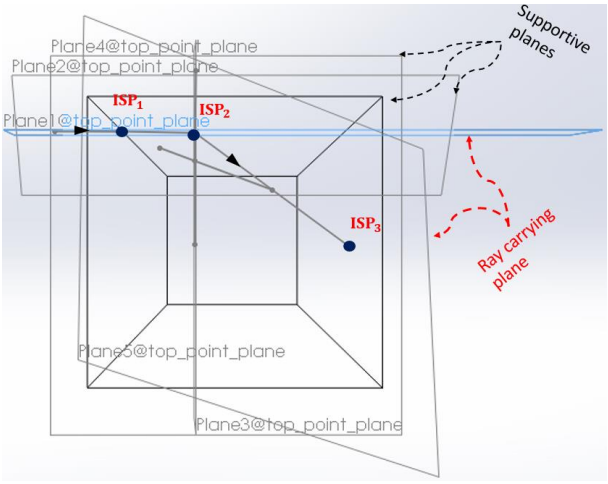

(c)

The RDP at the BRS is enriched with details from the various ray situations, however, these details are not sufficient to track the rays' paths from the TIS to the BRS at varied sun incidence angles. Tracing these routes is crucial for understanding the energy loss points and the reasons behind them. Additionally, the important of this analysis is to understand the optical behaviour of the system and optimizing its efficiency. For more clarity and to provide a comprehensive dataset for analysis, the numerical values representing the RDP are meticulously compiled in Table B.1.1, located in Appendix B. This problem is solved using a CAD model for the FPSRS, with a foundational assumption that the number of rays entering at the TIS is fixed at 100. This model facilitates a focused study on the trajectories that rays undertake within the system, with a particular emphasis on accurately determining the intersection points upon the reflectors. Such precision is essential for refining the design and enhancing the system's performance.

Out of the initial 100 rays, four are identified as critical for demonstrating the effect of minor deviations in the angle of incidence can drastically alter a ray's trajectory, potentially leading them to be lost from the system. These instances are significant as they highlight the sensitivity of the system to alignment and orientation, underscoring the importance of precision in the design and installation of the FPSRS. In accordance with this, first, the results highlighting the importance of reflectors by showing the intersection points on the reflectors are presented in Fig. 4.7. The FPSRS setup is assumed to have azimuthal alignment for all cases and reflector R3 facing the sun directly for all the value of θ. Moreover, the red arrow in Fig. 4.7 indicates the direction of the sun's rays (which will be from left to right). It is found from Fig. 4.7 that when rays are at θ = 30°, only type-D rays contribute towards collector efficiency.

It is observed that the full part of reflector R1 and a majority bottom portion of reflectors R2 and R4 remain blank or have no occurrence of any ray intersection. This is due to reflector R1 actually blocking most of the surfaces of the rest of the reflectors. The occurrence of direct rays

reaching the BRS starts from 50° onwards and reaches its maximum value at 90°. The subsequent sections aim to validate the experimental observations by correlating them with the outcomes derived from the CAD model, and by drawing parallels with findings from similar studies in the field. This comparative analysis is instrumental in affirming the reliability and accuracy of the experimental results, thereby enhancing the credibility of the study.

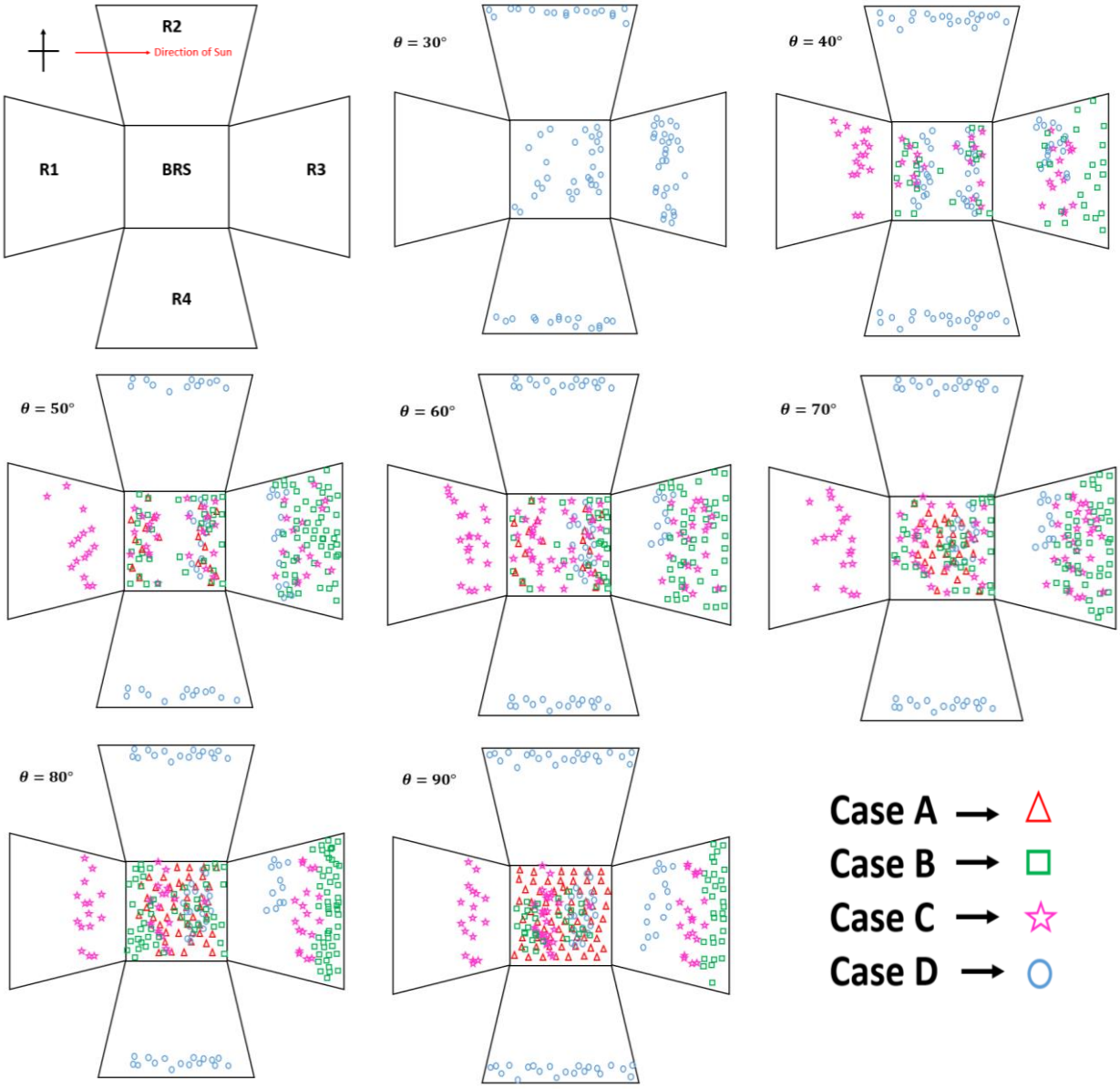

Fig. 4.7 Instances of occurrences of rays from A to D on the FPSRS for different solar incident angle.

4.3 Results and discussion

The observations from both the experimental study and CAD modelling are presented and validated in the present section. Additionally, the uncertainty analysis and thermal performance of the

system are discussed to gain real insights. As discussed earlier, the detailed coordinates and paths travelled by the selected four rays are documented in the Appendix B, offering vital insights into the system's behaviour under varied conditions.

4.3.1 Validation of results

Present section discusses the quantification of the error resulting from the experiment and its interpretation. It is essential to quantify the methods used to perform the experiment and the computed error as this will help validate the testing procedure followed and quantify its effectiveness. If error is under control the present method can be extended to analyse other types of reflector geometry as well, e.g. having TIS in the shape of hexagonal, octagonal, decagon, etc. Herein, first the single ray tracing experimental methodology is validated with the already performed experiment by A. C. Andre et al. (Carrillo-Andrés et al., 2022) on solar funnel cooker with considering shadow type tracing methodology. The Fig. 4.8 shows the results of comparative study for the optical performance of present experimental study and the experiments perform with consideration of shadow type tracing method. From the result it is observed that there is a good agreement between the results.

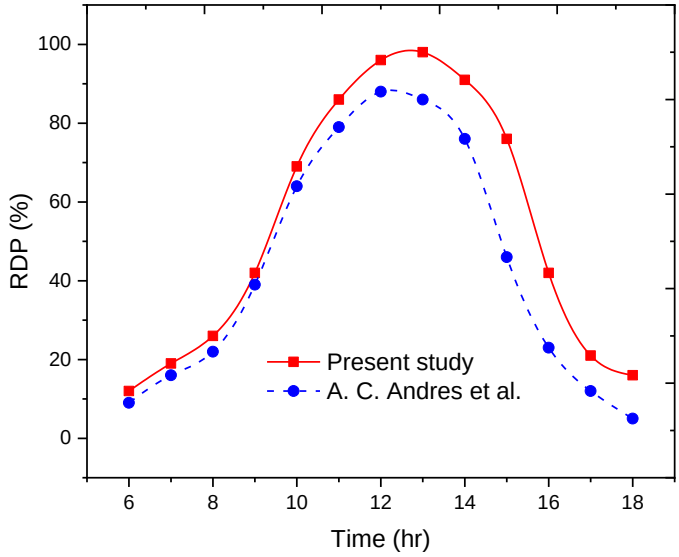

Fig. 4.8 Comparative study of the optical performance of present study and the experimental work (Carrillo-Andrés et al., 2022)

In the following section, the measuring error present at the intersection points on the reflector is very important parameter to compute, as it reflects the sensitivity of the model. As previously mentioned in section 4.2.3, four critical rays have been selected from all six different cases (A to F). The calculations have been performed for incident angles ranging from 30° to 90°, as angles below 30° do not significantly contribute to the final output, as discussed in section 4.2.2. The most appropriate rays chosen for a better understanding of the error present in the coordinates at the reflectors, for all cases from A to F, are shown in Fig. 4.9. The $R_{an}$is represents the beam ray entering

from the TIS for the CAD model and n shows the number of rays. It is observed that the selection of the critical rays for the cases of A and B is quite easy to in experiment as well as in CAD model. However, the selection process is quite complicated and difficult as the number of reflections increases with the participation of more reflectors and it making observations in the experiments becomes quite complex. Hence, the selection of rays for cases C, E, and F is comparatively more challenging as it involves a greater number of reflections. The most difficult task is to select the rays for case D, as it includes reflections from neighbouring reflectors as well. A similar approach is followed while conducting the experiments and selecting specific categories of rays for comparing the results with the CAD model.

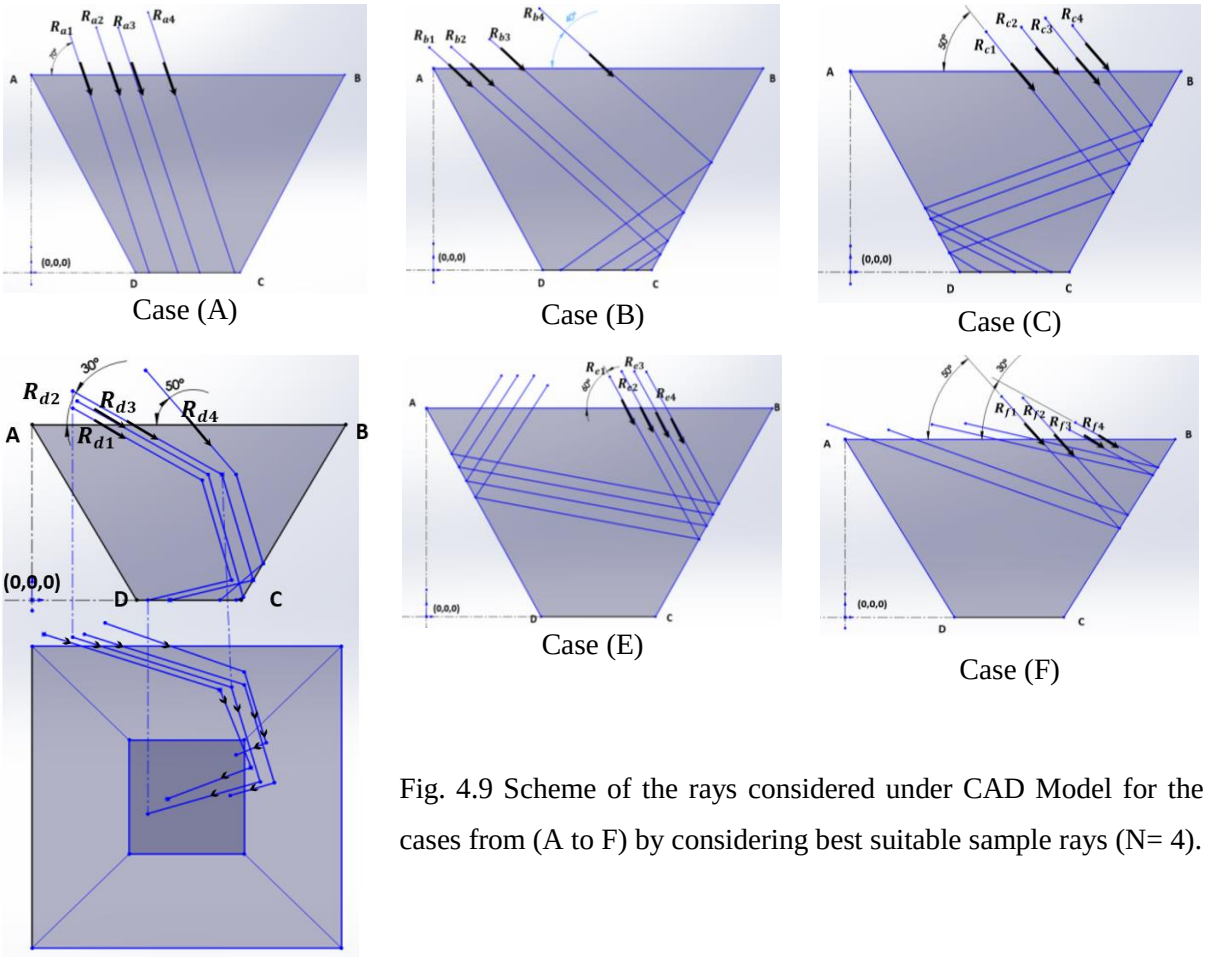

Fig. 4.9 Scheme of the rays considered under CAD Model for the cases from (A to F) by considering best suitable sample rays (N= 4).

This results in a total of 4 x 6 x 7 = 168 instances of rays taken into consideration for the error analysis. The dedicated experiments are conducted for each of these 168 rays and their coordinates are recorded systematically in Table B.1.2 in Appendix B. Additionally, the intersection points on reflectors from R1 to R4 are also recorded in Tables B.1.3, B.1.4, B.1.6 and B.1.7. In order to determine the path traced by each of these 168 rays, a simulated scenario is developed for these rays

in a CAD software. The path of each of such simulated rays is also recorded systematically and presented here as Table B.1.7. The final coordinates for these 168 rays reaching the BRS, obtained by both the types, i.e. path of rays tracked by conducting experiments and the same under simulated conditions using CAD software. All recorded data are logged, and the error in coordinates (E_r) is computed according to Eq. (4.2), with the results summarized in Table 4.3.

$$E_r = \frac{|(\text{Coordinate from CAD model} - \text{Coordinate from experiment model})|}{\text{Length of travel of the ray}} \times 100 \quad (4.2)$$

Table 4.3 shows the summary of the result of the error analysis for FPSRS. It is observed that the maximum amount of error observed is 3.1% in case-D type rays when the θ is 40º. One another fact is observed that the higher error occurred in a type of ray is attributed to its large travel length with more number of reflections, e.g. case D. In other words the errors can be under control if number of reflections are avoided and this is true especially for the reflectors involving very large value of OCR or small receiver area. Unlike this, the FPSRS are not highly sensitive to this type of error as it has a large size of receiver. The difference between the maximum and minimum values of E_r is referred to as the Maximum possible variation present in peak values and it is represented as 'δ_{max}'. The value of δ_{max} is computed with the help of Eq. 4.3.

$$\delta_{max}(\%) = E_{r\,(max)} - E_{r\,(min)} \quad (4.3)$$

Table 4.3 Value of E_r (%) observed for the rays reaching to the BRS [min, max]

θ	N	Case A	Case B	Case C	Case D
30º	1 to 4	-- *	-- *	-- *	1.6, 2.1
40º	1 to 4	-- *	0.2, 2.1	0.4, 1.5	0.36, **3.1**
50º	1 to 4	0.2, 0.2	0.3, 2.1	0.8, 2.2	0.7, 1.1
60º	1 to 4	0.5, 0.5	0.2, 1.3	0.2, 2.1	0.5, 1.8
70º	1 to 4	0.3, 1.1	0.4, 1.2	0.2, 2.0	0.2, 2.1
80º	1 to 4	0.1, 0.4	0.4, 1.2	0.2, 1.5	0.4, 2.2
90º	1 to 4	**0.1**, 0.3	0.3, 0.8	0.2, 1.6	0.2, 1.1

Note: * The cases shown with the dashed lines represent the rays not successful in reaching at the bottom.

Furthermore, to critically analyse the presence of E_r for a particular case of the ray and for a specific value of θ, the plot of δ_{max} along with the RDP for all possible values of θ is shown in Fig. 4.10. It is observed from the results that variation in δ_{max} is noted across different cases. Specifically, case A exhibits a very low value of δ_{max}, as these types of rays directly approach the BRS without

involving any reflections. In contrast, the value of δ_{max} in case B is higher compared to case A, as rays in this scenario experience one reflection before reaching the BRS. When comparing the maximum value of δ_{max} between cases B and C at 40°, it is noted that δ_{max} increases from case B to C. However, this trend is not consistent when θ is 50°. Additionally, at θ = 70°, δ_{max} attains a value that lies between the values for cases B and C. This variation could be explained by considering the error in assembling the structure or due to the alignment of the reflector planes relative to each other, which may have a compensating effect on E_r. In some instances, the impact of E_r may be negligible. This suggests that there could be some randomness in the trend, possibly due to the compensation of E_r when moving from case B to C. This might be attributed to potential errors in the angles of the reflectors, where the errors in two opposing reflectors may not have an additive effect. In the following discussion, the uncertainty analysis is presented for understanding the reliability of the system.

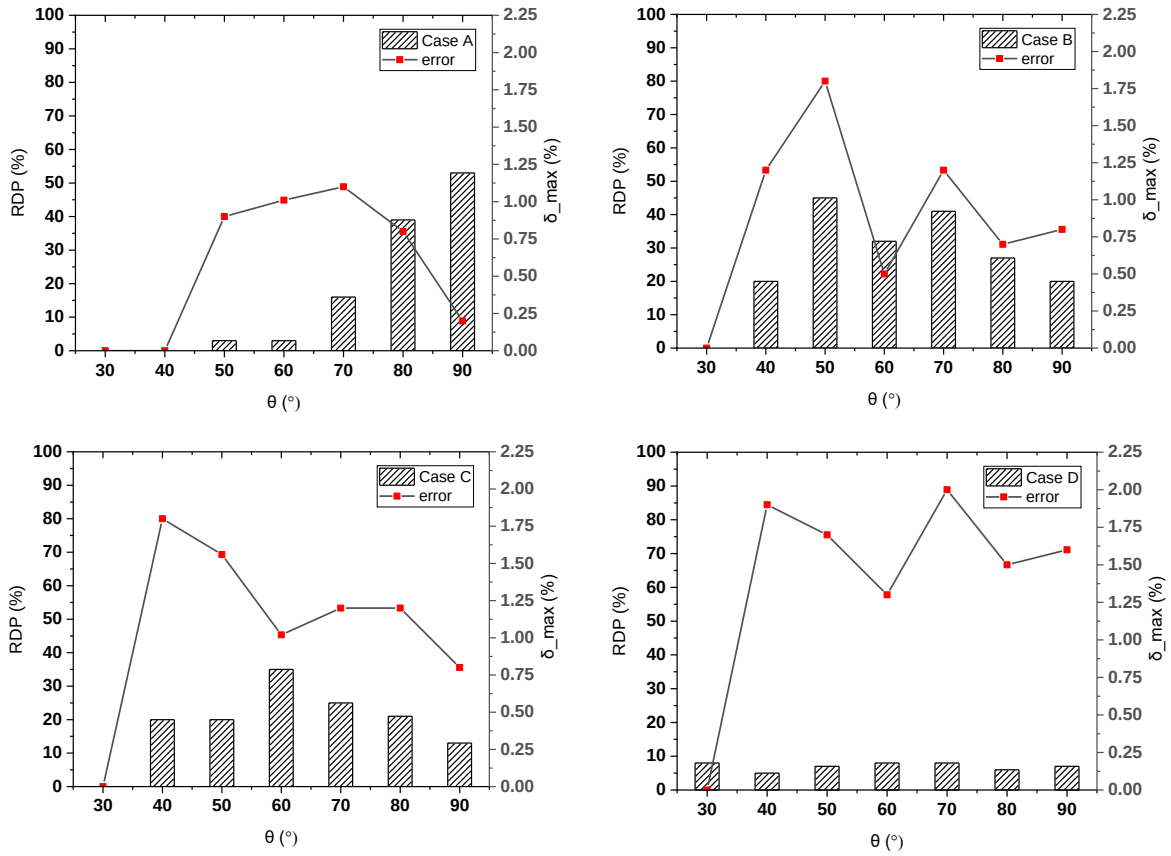

Fig. 4.10 Optical performance and δ_{max} for the cases from A to D of FPSRS

4.3.2 Uncertainty analysis

The Kline and McClintock method (Kline, 1985) for uncertainty analysis plays a critical role in assessing the reliability and sensitivity of the system. The uncertainty of the FPSRS is computed by using the mathematical expression shown in Eq. (4.4) with considering the RDP obtained at the BRS. This method prescribes the total uncertainty ($\Delta\chi$) as a function of the specific uncertainties present in the system's performance when analysing the behaviour of a single ray. However, in the literature, no such method for finding uncertainty while considering a single ray is available. Besides, the behaviour of the rays as discussed in the previous section, leads to the conclusion that the error in a particular ray is strongly influenced by minor changes in Φ. These minor change in the value of Φ by the reflector lead to significant variations when combining with other reflectors in the FPSRS as a whole. It's essential to address these sources of error to enhance the accuracy and reliability of FPSRS, particularly in applications where precision is critical, such as the single ray accountability is very important.

$$\Delta\chi = \sqrt{\left(\frac{\partial\chi}{\partial n_1}\cdot\Delta n_1\right)^2 + \left(\frac{\partial\chi}{\partial n_2}\cdot\Delta n_2\right)^2 + \cdots + \left(\frac{\partial\chi}{\partial n_n}\cdot\Delta n_n\right)^2} \tag{4.4}$$

There are many reasons for having an erroneous system, but the main reasons may include (a) errors during manufacturing or in fabricating funnel shape kind of the reflectors and (b) errors during the assembly of the FPSRS. Implementing rigorous quality control measures during manufacturing and assembly processes can help mitigate these errors, improve the overall performance and trustworthiness of FPSRS. To enhance the sensitivity of the system, both aforementioned errors are encompassed under uncertainty (χ) analysis. The severity of the value of χ can be assessed by considering two hypothetical reflectors with extreme levels of manufacturing inaccuracy. For this, the error in the angle of each side reflector due to cutting or joining the reflector is considered as $\Delta\Phi = 1°$, representing the maximum possible error. Fig. 4.11 illustrates a schematic depiction of the inaccuracy observed when reducing and ascending in angle (slope of the reflector). In the ideal case, $\angle AOB = 60°$ while in the actual case after considering errors of -1° and +1°, the angles become $\angle A'OB' = 58°$ (as shown in Fig. 11 (a)) and 62° (as shown in Fig. 11 (b)), respectively. This analysis highlights the significant impact of manufacturing inaccuracies on the overall performance and sensitivity of the system and it is emphasizing the importance of precision in reflector construction for optimal system functionality.

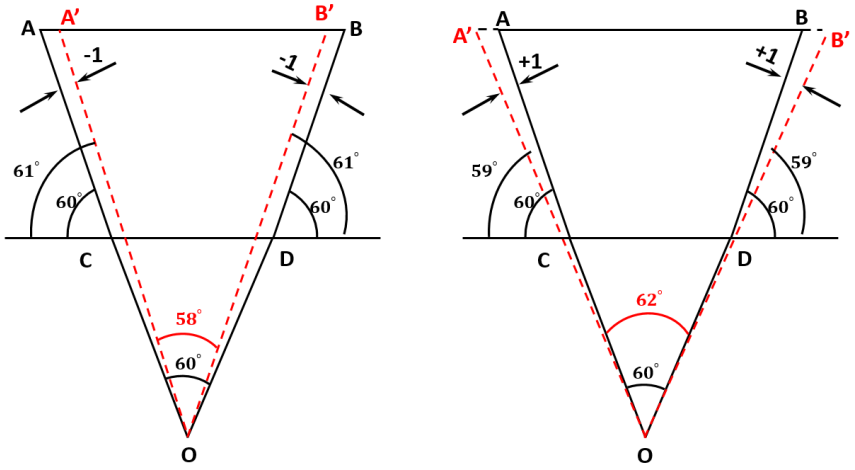

Fig. 4.11 Two hypothetical reflectors pyramid angle; (a) reduced by (-1) and (b) increased by (+1)

Figure 4.12 illustrates the uncertainty present with the help of error bars from case A to D and the results shows that there is significant variation particularly in cases C and D. The value of error is minimum in case A, followed by cases B, C, and D respectively. The maximum recorded errors are presented numerically in Table 4.4. Notably, the maximum uncertainty for both angles (58° and 62°) is calculated as 2.90% + 2.96% = 5.86% (for case D type ray), indicating higher uncertainty compared to other cases. This confirms the presence of a non-additive nature of errors in the experimental setup. Despite of this with considering the overall uncertainty value, it can be concluded that a similar setup like FPSRS can be reliable for STS and may be suitable for larger-scale applications.

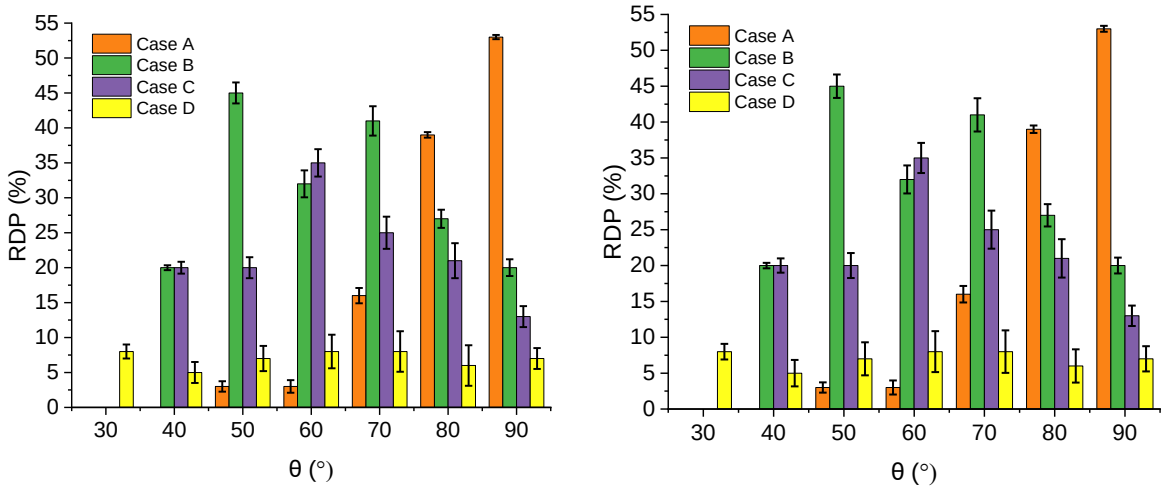

Fig. 4.12 Distribution of ray and corresponding value of χ for 58º (left) and 62º (right) geometry.

Table 4.4 Distribution of total χ when $\angle A'OB' = 58°$ and $\angle A'OB' = 62°$ respectively

θ	Case A	Case B	Case C	Case D
30º	-	-	-	1.00, 1.09
40º	-	0.35, 0.38	0.85, 1.00	1.50, 1.85
50º	0.75, 0.71	1.50, 1.63	1.50, 1.74	1.80, 2.30
60º	0.90, 0.98	1.93, 1.95	1.96, 2.10	2.40, 2.85
70º	1.10, 1.15	2.10, 2.32	2.30, 2.65	**2.90, 2.96**
80º	0.40, 0.52	1.30, 1.56	2.50, 2.68	2.90, 2.32
90º	0.30, 0.41	1.20, 1.10	1.50, 1.42	1.50, 1.76

4.3.3 Thermal performance of FPSRS

The thermal performance of FPSRS is analyse with considering consider three critical factors: a) ray scattering, b) path deflection and c) intensity weakening. However, among these three factors, the weakening of ray intensity, primarily caused by the reflector's poor reflectivity and significantly impacts the overall intensity of the reflected rays. This factor is crucial in understanding the system's thermal performance, as it directly influences the heat flux density at the BRS. Literature suggests that the average ρ of a well-maintained mirror stands at approximately 97% (Merrouni et al., 2015).

The η_{thr} of the FPSRS for the specific case with considering the relevant angle, is computed using Eq. 4.5. It is observed that considering the loss of thermal energy, each reflection leads to a 3% reduction in the radiative heat flux intensity of the ray. This means that for rays in case A, there is no deterioration or thermal loss. In case B, with a single reflection the thermal energy is reduced to 3%. For case C, having two reflections, the thermal loss will be accounted with number of reflection (ρ^n) and the value of its index n for the case A, B, C and D will be 0, 1, 2, and 2 respectively. An estimate of the thermal performance of the FPSRS can be made for a single day of operation, using solar radiation data as presented in Table 4.5.

$$\eta_{\text{thr}} = \sum_{\theta=30}^{\theta=150} \sum_{\text{Case = A}}^{\text{Case= D}} \text{DNI} * \text{Case} * \rho^{\text{n}} \quad (4.5)$$

The overall thermal performance of the FPSRS for all possible angles on a single day is shown in Fig. 4.13. The average value of η_{thr} is 69% while θ is ranging from 30° to 150°. It is noted that the η_{thr} is significantly high when θ is between 70° and 120° and beyond this it decreases rapidly on both sides of the curve. This sharp decline is due to the inclined rays and their reduced contribution to the reflector's efficiency. At θ = 90°, the η_{thr} is observed to be 91%, indicating that with full tracking of the reflector. This implies that the loss in efficiency due to the non-tracking of the reflector is only 22%. It is also observed that converting case B and case C into case A has a high

potential to further boost the FPSRS's efficiency. This enhancement can be achieved through appropriate design modifications, while case D has a very low potential to contribute and can be safely neglected in the overall efficiency calculation. Finally, the present experimental study provided foundational insights into the behaviour of single rays. However, a numerical investigation into the behaviour of rays can offer an in depth understanding that experimental methods alone may not capture.

Table 4.5 Solar radiation data for the location of Vadodara, Gujarat, India (April 2020)

θ^o	30	40	50	60	70	80	90	100	110	120	130	140	150
DNI	250	409	538	616	669	658	661	658	650	632	506	387	241

Source: Solcast https://solcast.com

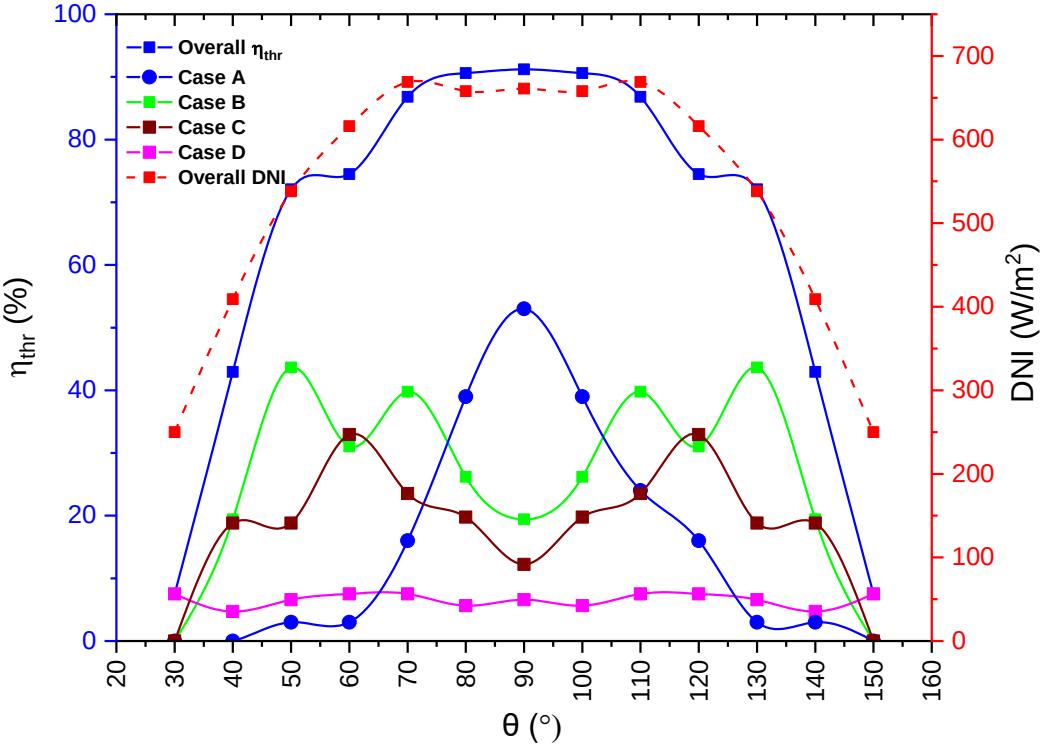

Fig. 4.13 Overall thermal performance of FPSRS

4.4 Summary

The present chapter highlights that FPTRs are cost-effective, easily accessible, and locally produced, making them advantageous for large-scale applications despite their lower efficiency compared to curved counterparts. The optical and thermal performance of the FPSRS was explored through a custom method for tracking the journey of a single ray. To enhance understanding of ray behaviour, the rays were categorized into six distinct cases (A to F), simplifying the experimental process and facilitating the study of individual beam behaviour.

The experiment of FPSRS was conducted in a dark room pointing a beam of laser light towards experimental model at varying incidence angles. The experimental findings with the single-ray experimental approach are in line with the earlier shadow experiment performed by A. C. Andres et al. (Carrillo-Andrés et al., 2022). The validated outcomes demonstrated that the currently proposed experimental procedure is both more reliable and feasible than traditional approaches. The critical behaviour of few rays were better understand with use of similar size of CAD model. The validation of CAD results and experimental results are under control. With use of the CAD model of FPSRS, the path of the rays and its intersecting coordinates can be easily measured with good accuracy. The findings show that the agreement between the experimental and CAD model has largest error occurring in case D which is order of 2.1%. The RDP results demonstrate that the contribution of rays belong to case A and case B increases with increase in the angle θ between 60° and 90°, and this leads to a highest contributors on the system's thermal performance.

The impact of the overall uncertainty effect is documented. It is observed that the maximum amount of uncertainty will not be beyond 5.8%. Overall uncertainty will be much reduced in actual case since the FPSRS will be 4 to 5 times larger than the scaled down model considered for the experiments. When θ is in the range of 30° to 150°, the derived average value of η_{thr} is 69%. The measured value of η_{thr} is 91% when θ is 90°, which suggests that the reflector can operate at its highest efficiency level if it is fully tracked. However this improvement contributes to overall η_{thr} only by 22%. This means thermal performance of FPSRS with a fixed reflectors and having azimuthal alignment will be 22% less compared to movable reflectors with azimuthal alignment. There is a possibility that expanding the reflectors' surface area will compensate for this loss.

The detailed analysis can be done with considering the numerical investigation of the similar kind of the study. These numerical studies are crucial for gaining detailed insights into the dynamics of ray reflection and their interactions with various surfaces, which is pivotal for optimizing the design and enhancing the efficiency of STSs. By complementing experimental data with numerical simulations, researchers can explore a wider range of conditions and configurations, potentially uncovering novel approaches to improve solar reflector performance. This integrated approach ensures a more comprehensive understanding of solar thermal systems, leading to more effective and efficient energy solutions.